Energy Storage Materials 52 (2022) 220–229

Contents lists available at ScienceDirect

Energy Storage Materials

journal homepage: www.elsevier.com/locate/ensm

3D artificial electron and ion conductive pathway enabled by MgH_2 nanoparticles supported on g-C_3N_4 towards dendrite-free Li metal anode

Hongyu Zhang [a,1], Yanran Wang [a,1], Shunlong Ju [a,1], Panyu Gao [a], Tongxin Zou [a], Tianren Zhang [b], Juan Wang [b], Guanglin Xia [a,*], Xuebin Yu [a,*]

[a] Department of Materials Science, Fudan University, Shanghai 200433, China
[b] Zhejiang Tianneng Battery Co., Ltd., Changxing 313100, Zhejiang, China

ARTICLE INFO

Keywords:
Li metal anode
Li dendrites
C_3N_4
Magnesium hydride
Full cells

ABSTRACT

Li metal anode is considered as one of the most promising candidates for next-generation batteries due to its high energy density. The undesired growth of Li dendrites and infinite volume change, however, hinders its practical application. Herein, a 3D structured Li metal anode featured with uniform electron and Li ion conductive pathway is fabricated through the favorable reaction between MgH_2 that are uniformly distributed on g-C_3N_4 and molten Li. The thus-formed lithiophilic LiMg alloys under the structural support of lithiophilc g-C_3N_4 could synergistically lower the nucleation barrier of Li plating and hence promote the uniform Li deposition process. Simultaneously, the high Li ion conductivity of thus-formed both LiH and Li_3N resulting from the reaction between molten Li and MgH_2 and g-C_3N_4, respectively, facilitates fast Li ion transportation kinetics along their surfaces towards favorable Li deposition on the surface of g-C_3N_4. Consequently, the thus-fabricated Li metal anode with a high specific capacity of 3511 mA h g^{-1} delivers a long cycling life of over 500 h at 3 mA cm^{-2} under 3 mA h cm^{-2}. Impressively, upon coupling this anode with commercial LFP cathode, the thus-assembled full cells deliver a specific capacity of 145 mA h g^{-1} after 450 cycles at 1 C.

1. Introduction

The increasing demand for energy density of Li-ion batteries (LIBs) promotes intensive investigation of Li metal anode due to its high theoretical specific capacity (3860 mA h g^{-1}) and redox potential (−3.04 V *vs* standard hydrogen electrode) [1, 2]. Moreover, Li metal anodes could be directly paired with Li-containing and Li-free cathodes (*e.g.*, oxygen and sulfur) to assemble next-generation batteries with high theoretical energy density than is over ten times that of current LIBs [3–5]. Despite these advantages, the uncontrollable growth of Li dendrites induced by the uneven Li nucleation and the formation of unstable solid electrolyte interphase (SEI) from the spontaneous reaction between Li metal and electrolyte lead to rapid capacity decay and limited lifespan [6–8]. More importantly, the infinite volume change of Li during repeated plating/stripping processes could easily break thus-formed fragile SEI layer, which hence aggregates the continuous formation of Li dendrites and "dead Li". The continuous growth of Li dendrites may lead to the penetration of the separator and cause short circuit and safety hazard, which severely hinders the practical application of Li metal anodes.

Accordingly, considerable efforts have been devoted to suppressing the uneven growth of Li dendrites and improving the stability of Li metal anodes. Among them, optimizing the composition of electrolyte with additives is able to stabilize Li metal anodes *via* the formation of stable SEI passivation layers [9–15]. Meanwhile, the stability of Li metal anodes could also be improved by building artificial protective layers, which could reduce the parasitical reaction and restrain the Li dendrite growth, and lithiophilic composites, which could effectively guide uniform nucleation and deposition of Li and induce dendrite-free Li plating performance [16–20]. Nevertheless, induced by the hostless nature of Li metal anode, the huge volume fluctuation during continuous Li plating and stripping process could easily deform or even destroy the fragile SEI layers and the modified surface, which aggravates side reactions between Li and electrolyte and hence the growth of Li dendrites, leading to severe degradation of cycling stability and even short circuit. As a result, designing conductive three-dimensional (3D) frameworks, which could

* Corresponding authors.
E-mail addresses: xiaguanglin@fudan.edu.cn (G. Xia), yuxuebin@fudan.edu.cn (X. Yu).
[1] Hongyu Zhang, Yanran Wang, and Shunlong Ju contributed equally to this work.

https://doi.org/10.1016/j.ensm.2022.08.001
Received 13 February 2022; Received in revised form 19 July 2022; Accepted 1 August 2022
Available online 5 August 2022

not only alleviate volume change during Li stripping/plating process, but also reduce local current density, have been widely proposed to restrain the formation of dendritic Li and improve the cycling stability of Li metal anodes [21–26]. Unfortunately, the introduction of inactive 3D hosts would add extra weight to Li metal anode and hence result in the sharp decrease of energy density. Moreover, due to the slow diffusion kinetics of Li ions inside the interior of 3D hosts, the growth of Li mainly occurs on the surface of Li metal anode, rather than inside the 3D hosts, especially at a high current density [27, 28]. It weakens the capability of 3D hosts in buffering the large volume change and reducing the local current density, which hence leads to the uneven plating of Li and the growth of Li dendrites upon long-term cycling process. Although the uneven growth of Li dendrites could be alleviated to some extent by enhancing the lithiophilicity of 3D hosts, the Li plating and stripping at the area away from the interface between 3D hosts and Li metal is still lack of control. Therefore, it is still a great challenge to stabilize Li metal anode under high current density towards long-term cycling performance.

Herein, taking advantage of MgH_2 nanoparticles (NPs) that are uniformly distributed on g-C_3N_4 (denoted as MgH_2@g-C_3N_4) as a structural platform, a 3D structured Li metal anode featured with favorable electronic and Li ion conductive pathways is built to suppress the formation of Li dendrites (Fig. 1a). Induced by the favorable reaction between MgH_2@g-C_3N_4 and molten Li, the simultaneous formation of lithiophilic LiMg alloys and LiH and Li_3N with high Li ion conductivity that are homogeneously distributed inside of the lithiophilic g-C_3N_4 as the structural support could be facile realized (denoted as LiMg-LiH@C_3N_4). The uniform formation of lithiophilic LiMg alloys with high solubility of Li under the structural support of lithiophilic g-C_3N_4 could synergistically lower the nucleation barrier of Li plating and hence

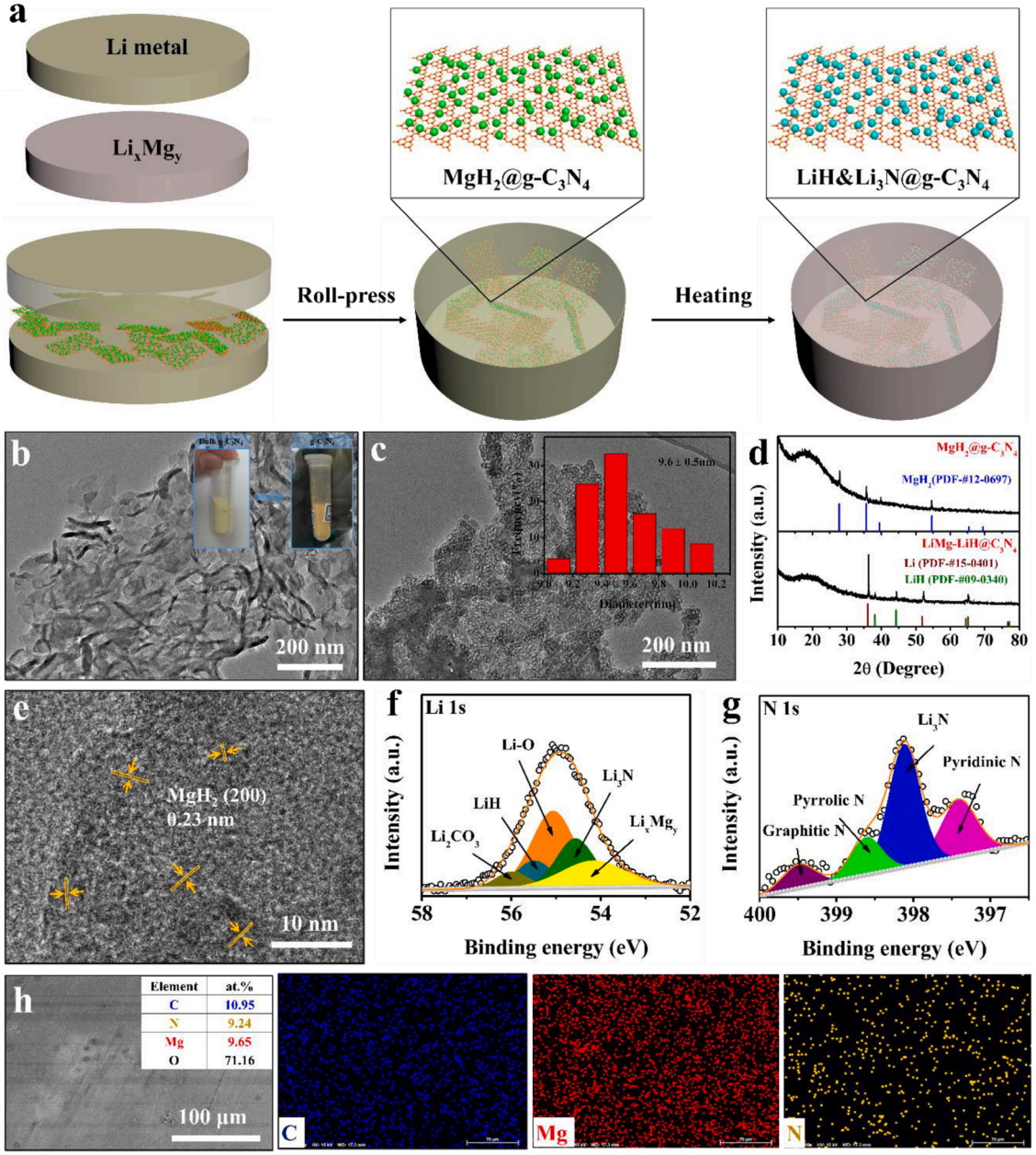

Fig. 1. (a) Schematic illustration for the fabrication of LiMg-LiH@C_3N_4 anode. (b) TEM image of g-C_3N_4 and the digital photograph of g-C_3N_4 powder (inset). (c) TEM image with the corresponding particle size distribution pattern (inset) of MgH_2@g-C_3N_4. (d) XRD patterns of the as-synthesized MgH_2@g-C_3N_4 and LiMg-LiH@C_3N_4. (e) HRTEM image of MgH_2@g-C_3N_4. (f) Li 1 s and (g) N 1 s XPS spectra of LiMg-LiH@C_3N_4. (h) Elemental mapping results of LiMg-LiH@C_3N_4 with atomic content of each element shown in the inset.

facilitate the uniform Li deposition process of LiMg-LiH@C_3N_4 anode. More importantly, owing to high Li ion conductivity of both LiH and Li_3N that are uniformly formed through the reaction between molten Li and MgH_2 and g-C_3N_4, the Li ion diffusion kinetics along their surfaces are thermodynamically favored towards favorable Li deposition on the surface of lithiophilic g-C_3N_4. In addition, the structural support role of the uniform distribution of g-C_3N_4 is capable of mitigating the large volume change during repeated Li stripping and plating process and hence stabilizing the formation of SEI layers. As a result, the as-fabricated LiMg-LiH@C_3N_4 anode with a high specific capacity of 3511 mA h g^{-1} delivers a long cycling life of over 500 h at a high current density of 3 mA cm^{-2} with a fixed capacity of 3 mA h cm^{-2}. More importantly, when coupling LiMg-LiH@C_3N_4 anode with commercial $LiFePO_4$ (LFP; 10.5 mg cm^{-2}) cathode, the thus-assembled full cell could deliver a specific capacity of 145 mA h g^{-1} after 450 cycles at 1 C, corresponding to a capacity retention of 94.2%. Moreover, the assembled full cells by coupling LiMg-LiH@C_3N_4 anode with commercial $LiNi_{0.8}Co_{0.1}Mn_{0.1}O_2$ (NCM811; 10 mg cm^{-2}) cathode exhibit stable cycling performance of over 450 cycles at 1 C, whereas a sharp decrease of capacity could be observed for the full cell using bare Li metal as the anode under identical condition after only 160 cycles.

2. Results and discussion

First, g-C_3N_4 nanosheets, which exhibit characteristic peaks in the X-ray diffraction (XRD) results (Fig. S1) with a typical stacked-layer structure as verified by transmission electron microscopy (TEM) image (Fig. 1b), are synthesized based on the self-polymerization of urea [29]. Subsequently, MgH_2 NPs supported on g-C_3N_4 (denoted as MgH_2@g-C_3N_4) are fabricated according to the hydrogenation-induced self-assembly process [30]. Scanning electron microscopy (SEM) (Fig. S2) and TEM images validate the uniform distribution of MgH_2 NPs with an average particle size of 9.6 nm on the surface of g-C_3N_4 (Fig. 1c). In the XRD pattern of MgH_2@g-C_3N_4 (Fig. 1d), the crystalline size of MgH_2 is calculated to be approximately 3.95 nm according to Debye-Scherrer equation, indicating that each MgH_2 nanoparticle is composed of 2~3 MgH_2 crystalline grains. In addition, high-resolution TEM (HRTEM) image verifies the presence of characteristic *d*-spacings of MgH_2 (Fig. 1e), which confirms the formation of MgH_2, corresponding well with the XRD and X-ray photoelectron spectroscopy (XPS) results (Fig. S3). Based on the hydrogen desorption amount, the loading capacity of MgH_2 is calculated to be approximately 50% (Fig. S4). Subsequently, the 3D structured Li metal anode is fabricated by mixing MgH_2@g-C_3N_4 and Li foil with various mass ratio by facile rolling and pressing for several times followed by thermal heating (denoted as LiMg-LiH@C_3N_4). After the reaction of MgH_2@g-C_3N_4 with Li metal, the characteristic peaks of LiH and LiMg alloys could be clearly observed, indicating the proceeding of the conversion rection between MgH_2 and molten Li. In the magnified XRD pattern (Fig. S5), the main peaks of LiMg alloys shift to higher angles compared with Li, which demonstrate the formation of Li-rich solid-solution LiMg alloys with a body-centered cubic (*bcc*) structure. The peaks at 55.5 eV and 54.1 eV in high-resolution Li 1 s XPS spectra, which could be indexed to LiH and LiMg alloys, respectively, provide additional evidence to the formation of LiH and LiMg alloys. Interestingly, an extra peak at 54.5 eV that could be indexed to Li_3N is clearly detected, indicating the formation of Li_3N induced by the favorable reaction between molten Li and g-C_3N_4 (Fig. 1f). The presence of Li_3N could be further supported by the presence of the characteristic peak of Li_3N at 398.1 eV in the N 1 s XPS spectra (Fig. 1g), in which the characteristic peaks of N-$(C)_3$ groups and C—N=C groups in the tri-s-triazine units of g-C_3N_4 could also be detected. The energy dispersive X-ray spectroscopy (EDX) mapping results (Fig. 1h) reveal the homogeneous distribution of C, N, and Mg inside of the whole electrode, demonstrating uniform distribution of MgH_2@g-C_3N_4 into Li metal, which could be attributed to the thermodynamically favored reaction of both g-C_3N_4 and MgH_2 with molten Li. After stripping away all active Li metal, the 3D structure composed of uniformly dispersed g-C_3N_4 sheets encapsulated with Li-poor LiMg-g-Li_3N-LiH nanoparticles is maintained (Fig. S6a and b). This result further demonstrates that the structure and morphology of g-C_3N_4 could be well preserved after partial reaction with Li, and solid-solution LiMg alloys could be uniformly confined into 3D structured g-C_3N_4-Li_3N-LiH.

The nucleation overpotentials for Li plating, a key indicator for estimating the lithiophilic degree of the electrode, is first investigated to reveal the role of LiMg-LiH@C_3N_4 in suppressing the growth of Li dendrites (Fig. S7). Based on the difference between the tip potential and the later stable voltage, a nucleation overpotential of 61 mV could be observed for bare Li metal anode, which demonstrates the presence of large nucleation barrier for Li plating into pristine Li metal [31]. The introduction of either g-C_3N_4 (denoted as Li@C_3N_4) or MgH_2 NPs (denoted as LiMg-LiH) into Li metal could effectively lower the nucleation overpotential of Li plating down to 24 and 27 mV, respectively, indicating the lithiophilic nature of g-C_3N_4 and LiMg alloys, which could be verified by the theoretical simulations based on density functional theory (DFT) calculations. The binding energy between Li and the thus-formed LiMg alloys from the reaction between MgH_2 and Li could reach −1.7 eV (Fig. 2a), slightly lower than that for Li metal (−1.4 eV) [32], and moreover, this value could be significantly decreased to −3.5 eV for g-C_3N_4 (Fig. 2b). As a result, the introduction of LiMg alloys and g-C_3N_4 is able to effectively lower the nucleation barrier of Li plating, which hence could facilitate the homogeneous nucleation of Li metal and hinder the formation of Li dendrites. Accordingly, induced by the co-existence of g-C_3N_4 and MgH_2 NPs, the nucleation overpotential of LiMg-LiH@C_3N_4 is further reduced to 17 mV, which provides direct evidence to the synergistic role of MgH_2 and g-C_3N_4 of MgH_2@g-C_3N_4 in facilitating Li plating process.

The electrochemical performance of LiMg-LiH@C_3N_4 anode is initially investigated in symmetric cells at 1 mA cm^{-2} with a fixed areal capacity of 1 mA h cm^{-2} (Fig. 2c), with bare Li, Li@C_3N_4, and LiMg-LiH electrode included for comparison. The voltage hysteresis exhibits an obvious increase after only 290 h for bare Li anode due to the continuous increase of interfacial impedance resulting from the rapid corrosion of Li metal by electrolytes and the growth of Li dendrites. After the modification with g-C_3N_4, the symmetric cells of Li@C_3N_4 deliver stable cycling in the initial 485 h, confirming the positive role of g-C_3N_4 in suppressing the growth of Li dendrites. It could be attributed to both the lithiophilic nature of g-C_3N_4, which regulates the uniform Li plating process, and the formation of Li_3N with high Li ion conductivity, which promotes uniform transportation of Li ion across the whole electrode [33–35]. Unfortunately, upon the proceeding of cycling Li stripping and plating process, the voltage hysteresis gradually increases after 500 h and reaches 80 mV after 900 h. By comparison, the LiMg-LiH@C_3N_4 anode could operate stably for over 1100 h without obvious increase of overpotentials, suggesting the synergistic role of g-C_3N_4 and MgH_2 NPs in effectively stabilizing Li metal anode. In addition to the effect of g-C_3N_4 in enhancing stability of Li metal anode, the positive role of MgH_2 in stabilizing Li metal anode could be attributed to the lithiophilic nature of thus-formed LiMg alloys. Various amounts of MgH_2@g-C_3N_4 were investigated. When the content of MgH_2@g-C_3N_4 is only 2.5 wt.%, the contents of lithiophilic LiMg alloys and g-C_3N_4, and Li ion conductor (Li_3N and LiH) are low, which is not favorable for uniform Li deposition and good cycling stability. Meanwhile, when MgH_2@g-C_3N_4 contents are increased to 7.5 and 10 wt.%, g-C_3N_4-Li_3N-LiH may not disperse uniformly in the whole electrode (Fig. S8 and S9), which could induce heterogeneous Li deposition and thus poor cycling performance. Therefore, the weight percent of MgH_2@g-C_3N_4 was optimized to be 5 wt.% (Fig. S10). Interestingly, upon using Mg@g-C_3N_4 as the structural support, which would prevent the formation of LiH upon the reaction with Li, although the nucleation overpotential could also be largely decreased owing to the presence of both LiMg alloys and g-C_3N_4 as the lithiophilic sites, the cycling stability of Li metal anode is degraded compared with MgH_2@g-C_3N_4 (Fig. S11). This result directly

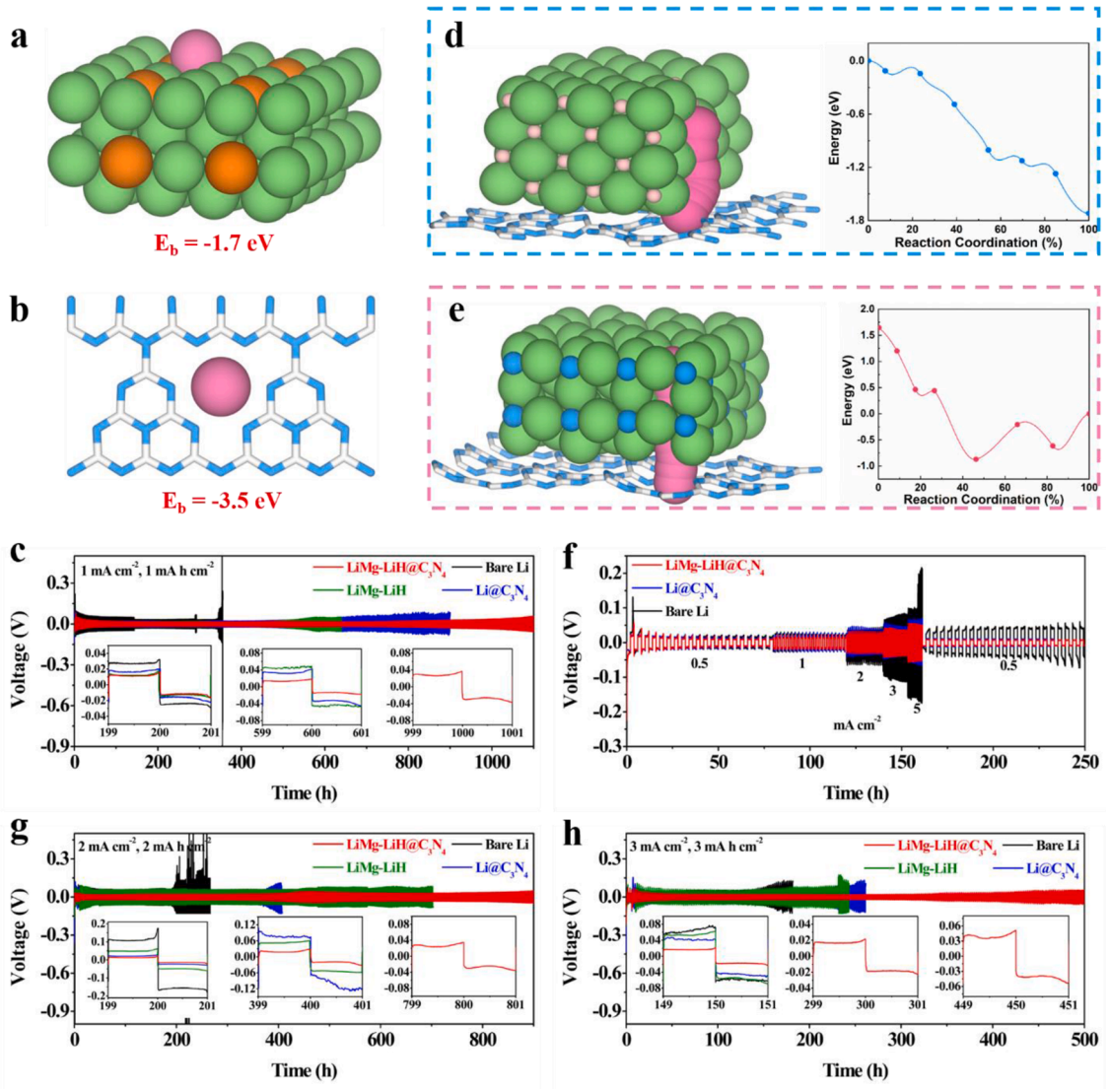

Fig. 2. The adsorption configuration of Li on (a) Li_7Mg (001) surface and (b) g-C_3N_4. (c) Galvanostatic discharge/charge voltage profiles of the LiMg-LiH@C_3N_4 in symmetric cells at 1 mA cm^{-2} with a fixed capacity of 1 mA h cm^{-2}, with LiMg-LiH, Li@C_3N_4, and bare Li anode included for comparison. The diffusion pathway and calculated energy profile of Li along the diffusion path of (d) LiH and (e) Li_3N towards Li plating on the surface of g-C_3N_4. (f) Rate performance of LiMg-LiH@C_3N_4, Li@C_3N_4, and bare Li electrode in symmetric cells. The orange, green, blue and light pink balls denote Mg, Li, N and H atoms, respectively. The deep pink balls stand for Li atoms in adsorption or diffusion configuration. Galvanostatic discharge/charge voltage profiles of the LiMg-LiH@C_3N_4, LiMg-LiH, Li@C_3N_4, and bare Li electrode in symmetric cells (g) at 2 mA cm^{-2} with a fixed capacity of 2 mA h cm^{-2} and (h) at 3 mA cm^{-2} with a fixed capacity of 3 mA h cm^{-2}.

demonstrates that the presence of LiH with high Li ion conductivity also plays an important role in regulating the homogeneous Li plating behavior. Therefore, in addition to lithiophilic property, the Li ion diffusion behavior of LiMg-LiH@C_3N_4 anode is investigated by theoretical calculation. As shown in Fig. 2d and e, with the assistance of LiH and Li_3N resulting from the reaction between molten Li and g-C_3N_4 and MgH_2 NPs, respectively, the Li diffusion along both LiH and Li_3N down to the surface of lithiophilic g-C_3N_4 towards Li plating is thermodynamically favored without observation of any obvious energy barrier. It validates the presence of LiH and Li_3N that is uniformly distributed inside of LiMg-LiH@C_3N_4 anode could promote the fast Li ion diffusion on their surfaces towards favorable Li plating. This result could be experimentally supported by the exchange current density (I_0) of LiMg-LiH@C_3N_4 anode that is much higher than that of both Li@C_3N_4 and bare Li metal anode before and after cycling process (Fig. S12), which provides direct evidence to the significantly enhanced interfacial transport of Li ion owing to the simultaneous formation of LiH and Li_3N induced by the homogeneous introduction of MgH_2@g-C_3N_4. Hence, it is concluded that the homogeneous introduction of both g-C_3N_4 and MgH_2 with uniform distribution play an important role in enhancing both lithiophilic property and the Li ion diffusion of the whole electrode, which effectively suppresses the formation of Li dendrites owing to the lithiophilic nature of both C_3N_4 and LiMg alloys and the high Li ion conductivity of Li_3N and LiH.

In order to develop rechargeable batteries with high energy/power density, the cycling stability at high operating current densities with high areal capacities, which in general would aggravate the formation of Li dendrites and dead Li, should be measured [36, 37]. The rate performance of LiMg-LiH@C_3N_4 anode are further tested at various current densities with a fixed areal capacity of 1 mA h cm^{-2} (Fig. 2f). The LiMg-LiH@C_3N_4 anode shows a steady voltage polarization value of 12, 17, 28, 35, and 49 mV at the current density of 0.5, 1, 2, 3, and 5 mA cm^{-2}, respectively. When the current density drops back to 0.5 mA cm^{-2}, the voltage value reinstates a lower value of ~10 mV, indicating the excellent reversibility of LiMg-LiH@C_3N_4 anode. By comparison, symmetric cells of bare Li metal present a larger voltage hysteresis, particularly at high current densities. Long-term cycling performance illustrates that the symmetric cells with pristine Li anode exhibit severe

increase of voltage hysteresis with dramatic fluctuation at 2 mA cm^{-2} with a fixed capacity of 2 mA h cm^{-2} after only 200 h. Although the cycling stability of Li metal anode could be enhanced to some extent *via* the modification of g-C_3N_4, the overpotential of Li@C_3N_4 is still increased to 60 mV after only 380 h. In strong contrast, the thus-fabricated LiMg-LiH@C_3N_4 anode exhibits stable cycling performance with a low overpotential of only ~30 mV after 890 h under identical condition (Fig. 2g). More importantly, when the current density is increased to 3 mA cm^{-2} and the capacity is fixed at 3 mA h cm^{-2}, LiMg-LiH@C_3N_4 anode is still capable of operating stably with low overpotential for 500 h (Fig. 2h).

To visually investigate Li stripping and plating behavior, the morphology of LiMg-LiH@C_3N_4 after Li stripping and plating are detected. As shown in Fig. S13, obvious pits could be observed for bare Li metal anode after stripping 2 mA h cm^{-2} of Li at 1 mA cm^{-2} and inhomogeneous plating of Li with the presence of cracks is clearly detected on the surface of Li metal after the reversible Li replating process, which directly demonstrates the uneven Li stripping and plating process of pristine Li metal. The increase of Li stripping and plating capacity to 5 mA h cm^{-2} could largely exacerbate the growth of pits and the irregular Li plating behavior (Fig. 3b and c). As a result, upon the proceeding of Li plating and stripping process, mossy Li and numerous cracks is clearly observed for bare Li metal anode with the observation of Li dendrites and "dead Li" after 50 cycles (Fig. 3d), which could lead to penetration of electrolyte and accelerate the side reaction between electrolyte and fresh Li underneath to consume residual Li metal. Although this phenomenon could be alleviated to a large extent due to the uniform introduction of g-C_3N_4 with excellent lithiophilic nature and the thus-induced formation of Li_3N with high Li ion conductivity, the formation of pits and holes and the reversible formation of irregular Li grains could still be observed occasionally on the surface of Li@C_3N_4 (Figs. 3e-h and S14). Meanwhile, with the introduction of Mg in Li metal to form lithiophilic solid-solution LiMg alloys, small amount of "dead Li" and a few cracks could also be observed on the LiMg alloys after 50 cycles (Fig. S15), which is responsible for its limited cycling performance [38, 39]. This may result from the absence of LiH and Li_3N to facilitate the Li ion diffusion inside LiMg alloys towards favorable Li plating and the lack of host to buffer the volume change during cycling. In strong contrast, the surface of LiMg-LiH@C_3N_4 remains smooth after Li stripping and plating at 1 mA cm^{-2} with a fixed capacity of 2 mA h cm^{-2} and more importantly, the smooth surface could be well preserved even after stripping and replating of 5 mA h cm^{-2} of Li at 1 mA cm^{-2} (Fig. S16 and Fig. 3i-k). It could be attributed to the enhanced kinetics of both electron and Li ion diffusion kinetics across the whole electrode induced by the introduction of MgH_2@g-C_3N_4. More importantly, a relatively uniform surface could still be obtained for LiMg-LiH@C_3N_4 anode after 50 cycles (Fig. 3l), Meanwhile, when all the active Li were stripped away, the 3D structure composed of Li-poor LiMg-Li_3N-LiH nanoparticles embedded in uniformly dispersed g-C_3N_4 sheets is still well maintained after 50 cycles (Fig. S6c and d), which demonstrates the structure and morphology could be well preserved after repeated Li stripping/plating process. These results indicate the capability of LiMg-LiH@C_3N_4 anode in withstanding large volume change during Li plating and stripping process, which could be attributed to the structural support role of g-C_3N_4 that is uniformly distribution inside of LiMg-LiH@C_3N_4 anode. Furthermore, elemental mapping results validate the homogeneous distribution of Mg, C, and N element in the whole matrix of the cycled LiMg-LiH@C_3N_4 anode, which demonstrates the stable structural integrity of the whole electrode with well distribution of C_3N_4 and LiMg alloys as the lithiophilic sites and LiH and Li_3N as the Li ion conductors (Fig. 3m). It is able to effectively suppress the formation of Li dendrites and hence improve the cycling stability of LiMg-LiH@C_3N_4 anode.

Electrochemical impedance spectrum (EIS) measurements are subsequently carried out to investigate the interfacial charge transfer of symmetric cells during cycling Li stripping and plating process. Detailed

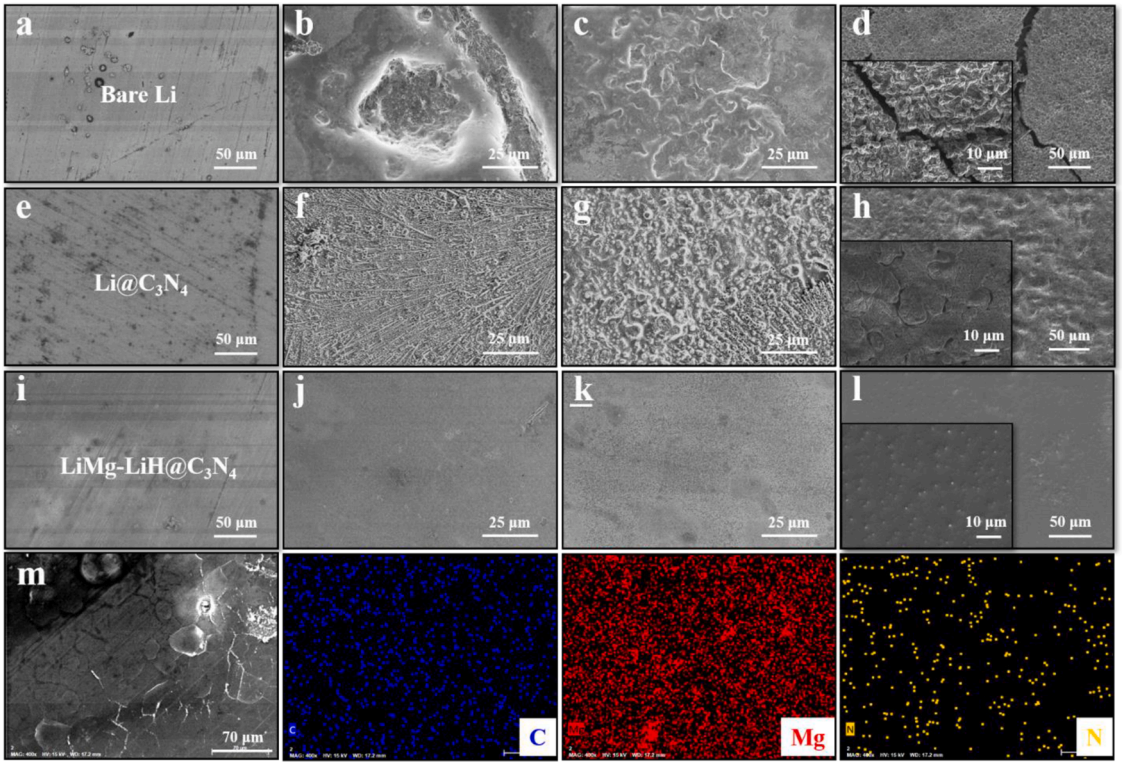

Fig. 3. SEM images of the (a-d) bare Li, (e-h) Li@C_3N_4, and (i-l) LiMg-LiH@C_3N_4 (a, e, i) before cycling, (b, f, j) after stripping 5 mA h cm^{-2} of Li at 1 mA cm^{-2}, (c, g, k) after stripping of 5 mA h cm^{-2} and replating 5 mA h $cm^{-2}$of Li at 1 mA cm^{-2} and (d, h, l) after 50 cycles at 1 mA cm^{-2}, 1 mA h cm^{-2}, respectively. (m) SEM image and the corresponding elemental mapping results of LiMg-LiH@C_3N_4 after 100 cycles.

fitting results exhibit that both SEI resistance (R_{SEI}) and the interfacial charge transfer resistance (R_{ct}) of LiMg-LiH@C_3N_4 anode is obviously lower than that of both Li@C_3N_4 and bare Li metal anode, suggesting the improvement of electronic conductivity due to the introduction of MgH_2@g-C_3N_4 (Fig. S17 and Table S1). Although the decrease of R_{SEI} and R_{ct} could be observed for bare Li metal anode after 50 cycles of Li stripping and plating process, which should be attributed to the formation of Li dendrites with higher surface area that enhances the electrolyte contact, the continuous consumption of the electrolyte and the thickening of the SEI layers leads to the increase of R_{SEI} and R_{ct} to 34 and 14 Ω, respectively, after 100 cycles. Impressively, the 3D LiMg-LiH@C_3N_4 anode exhibit stable both R_{SEI} and R_{ct} during 100 cycles of Li stripping and plating process, much lower than that of bare Li metal anode, which indicates the improved interfacial stability of the whole electrode due to the suppressed formation of Li dendrites and dead Li. The interfacial stability of LiMg-LiH@C_3N_4 anode after 20 cycles is subsequently investigated by depth profiling of X-ray photoelectron spectroscopy (XPS) analysis *via* Ar ion etching (Fig. 4). It can be clearly observed that, the N 1 s spectra of LiMg-LiH@C_3N_4 anode at 398.3 eV, 398.9 eV, and 397.4 eV could be attributed to the Li_3N and the pyrrolic N and pyridinic N of g-C_3N_4, respectively. The Li 1 s peaks at 54.5 eV and 54.1 eV could be assigned to Li_3N and Li_xMg_y alloys, respectively, in accordance with N 1 s peak at ~398.3 eV and Mg 1 s peak at ~1303.0 eV, which provides additional evidence to the formation of Li_3N and Li_xMg_y alloys from the interaction between molten Li and g-C_3N_4. In addition, the peak at 684.7 eV in F 1 s spectrum and the peak at 56.0 eV in Li 1 s spectrum could be attributed to the formation of LiF, which results from the decomposition of LiTFSI from the electrolyte [40, 41]. It could be directly noticed that the surface of both bare Li and LiMg-LiH@C_3N_4 anode is mainly covered by LiH, Li-O-, LiF, and Li_3N, which are the common components of SEI layers that would be formed in ether-based electrolyte. Owing to the continuous formation of SEI layers induced by the growth of Li dendrites and dead Li, only negligible change of peak intensity of LiH, Li-O-, LiF, and Li_3N could be observed for bare Li metal anode upon the proceeding of etching (Fig. S18), suggesting the thickness of thus-formed SEI layers is much higher than 500 nm. In strong contrast, the obvious decrease of peak density of these major SEI components and the increase of peak density of LiMg alloys could be observed for the LiMg-LiH@C_3N_4 anode after cycling upon the increase of etching depth, which directly demonstrates the formation of stable SEI layers with a thickness that is much smaller than that of bare Li metal anode. These results verify that the facile construction of 3D structured LiMg-LiH@C_3N_4 anode *via* introducing MgH_2@g-C_3N_4 could not only promote the uniform Li stripping and plating process but also stabilize the formation of SEI layers, leading to the significantly enhanced cycling stability.

To validate the potential practical applications of the LiMg-LiH@C_3N_4 anode, full cells are constructed by coupling LiMg-LiH@C_3N_4 anode with commercial cathodes, *i.e.*, $LiFePO_4$ (LFP) and $LiNi_{0.8}Co_{0.1}Mn_{0.1}O_2$ (NCM811), for electrochemical investigation. The specific capacity of LiMg-LiH@C_3N_4 anode is first evaluated by galvanostatic charging to confirm the N/P ratio in full cells test (Fig. 5a), which exhibits a high specific capacity of 3511 mA h g^{-1} for LiMg-LiH@C_3N_4 anode (activated Li in LiMg-LiH@C_3N_4 anode: 90.9 wt.%), close to the theoretical specific capacity of Li. According to this result, the atomic ratio of active Li and Mg in the as-fabricated LiMg-LiH@C_3N_4 is calculated to be approximately 1000:7.4, which further demonstrates the formation of Li-rich solid-solution LiMg alloys. Furthermore, considering the reaction of $MgH_2 + 2Li \rightarrow Mg + 2LiH$, the mass ratio of LiMg alloys, LiH, and Li_3N in LiMg-LiH@C_3N_4 is estimated to be 93.3%, 1.6%, and below 4.4%, respectively. Rate capability performance validates that LiMg-LiH@C_3N_4||LFP full cell delivers a higher reversible specific capacity of 172, 162, 150, 133, and 110 mA h g^{-1} at 0.2, 0.5, 1, 2, and 4 C, respectively, much higher than that of bare Li metal anode, especially at high rates (Fig. 5b). The improved capacity of LiMg-LiH@C_3N_4||LFP full cell could be attributed to the superior Li ion transfer kinetics of LiMg-LiH@C_3N_4 as verified by the lower overpotential in the discharge and charge profiles at various current densities (Figs. 5c and S19). In addition, long-term cycling performance illustrates that the full cells assembled with the pristine Li metal as the anode and LFP (10.5 mg cm^{-2}, ~1.785 mA h cm^{-2}) as the cathode exhibit rapid capacity decay after only 200 cycles at 1 C, delivering a capacity retention rate of only 85.2% after 220 cycles. The capacity degradation could be ascribed to the formation of "dead Li" induced by repeated growth and isolation of Li dendrites (Fig. S20a and b), which always companied with the thickening of SEI and the consumption of active Li and electrolyte. By comparison, the assembled LiMg-LiH@C_3N_4||LFP full cells show stable cycling performance and a specific capacity of 145 mA h g^{-1} could still be obtained after 450 cycles, corresponding to a capacity retention of 94.2%, suggesting the formation of stable SEI layers between LiMg-

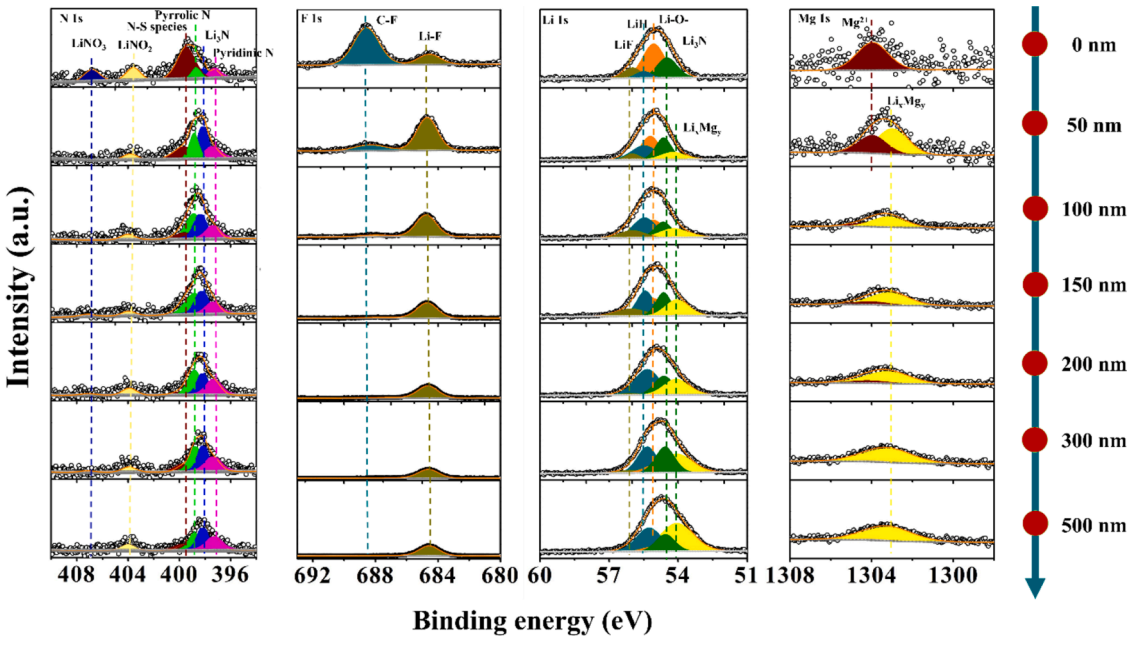

Fig. 4. XPS depth profile of LiMg-LiH@C_3N_4 electrode after 20 cycles at 1 mA cm^{-2} with a fixed capacity of 1 mA h cm^{-2}.

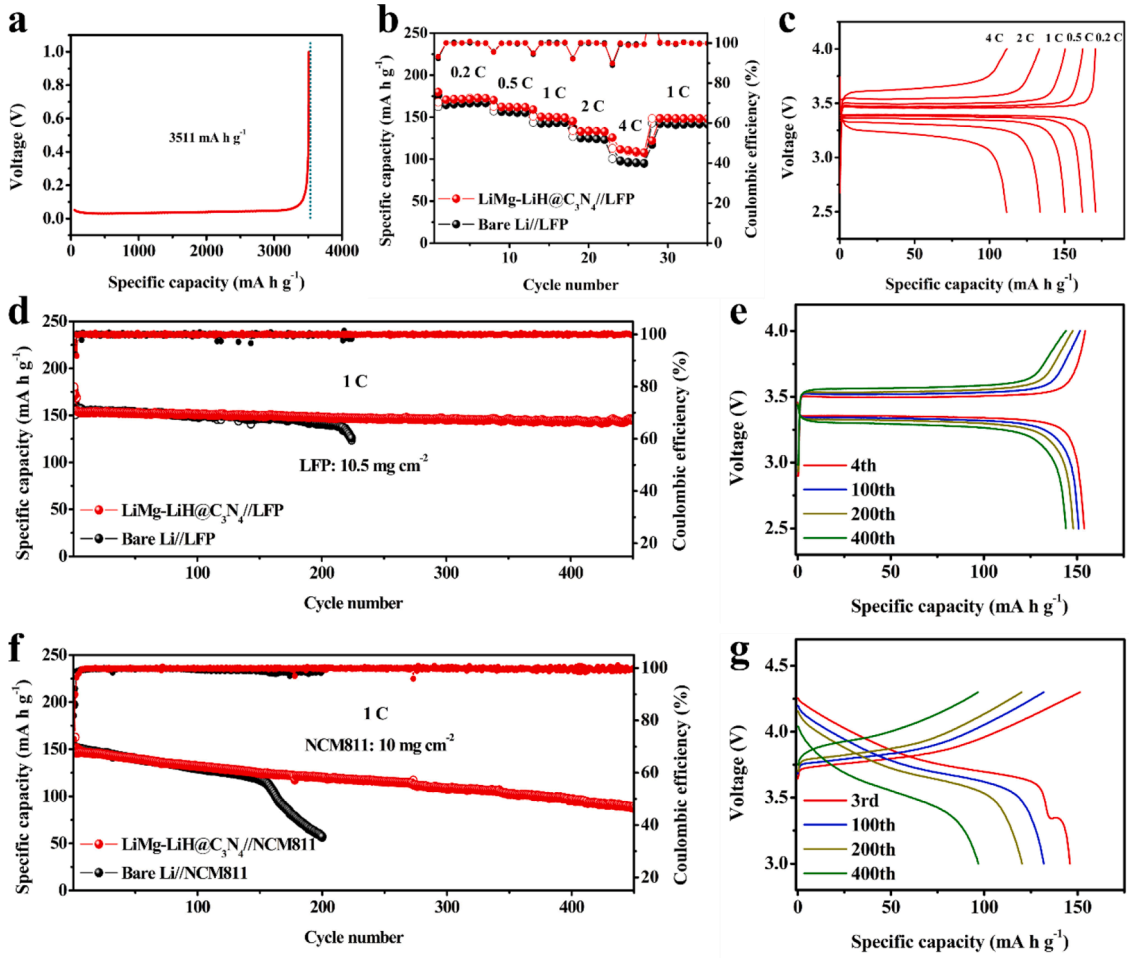

Fig. 5. (a) Galvanostatic charge profile of LiMg-LiH@C_3N_4 anode. (b) Rate capability profiles of bare Li||LFP and LiMg-LiH@C_3N_4||LFP full cells at various rates from 0.2 C to 4 C (1 C = 170 mA g^{-1} for LFP cathode). (c) Charge/discharge profiles of LiMg-LiH@C_3N_4||LFP full cell at various rates. (d) Cycling performance of bare Li||LFP and LiMg-LiH@C_3N_4||LFP full cells at 1 C. (e) Charge/discharge profiles of LiMg-LiH@C_3N_4||LFP full cell at 1 C. (f) Cycling performance of bare Li||NCM811 and LiMg-LiH@C_3N_4||NCM811 full cells at 1 C (1 C = 170 mA g^{-1} for NCM811 cathode). (g) Charge/discharge profiles of LiMg-LiH@C_3N_4||NCM811 full cell at 1 C.

LiH@C_3N_4 anode and electrolyte upon cycling. The excellent cycling performance could be further supported by the smooth and dense surface morphology of LiMg-LiH@C_3N_4 (Fig. S20c and d). In addition, a lower polarization could be observed for the LiMg-LiH@C_3N_4||LFP full cell that of the bare Li||LFP full cell during different cycles of charge and discharge process, indicating the well-preserved electron and Li ion conductivity of LiMg-LiH@C_3N_4 anode upon cycling (Figs. 5e and S21). To test the cycling performance at high rates, the current density was increased to 4 C (Fig. S22), bare Li||LFP full cells show rapid capacity decay after 150 cycles with a capacity retention of 13.2% after 300 cycles. In contrast, LiMg-LiH@C_3N_4||LFP full cells exhibit a stable cycling performance of over 500 cycles with a capacity retention of 81.3% due to the uniform deposition/stripping of Li and fast Li ion diffusion kinetics in LiMg-LiH@C_3N_4 electrode. The advantages of LiMg-LiH@C_3N_4 anode is further investigated by coupling with commercial NCM811 cathode (10 mg cm^{-2}, ~ 1.7 mA h cm^{-2}). Taking advantage of the uniform Li stripping and plating process, the thus-assembled LiMg-LiH@C_3N_4||NCM811 full cell delivers a high specific capacity of 89 mA h g^{-1} at 1 C after a long cycling life of 450 cycles, whereas a sharp decrease of capacity could be clearly observed for bare Li||NCM811 full cell under identical condition after only 160 cycles (Fig. 5f). In addition, induced by the well-preserved stability of LiMg-LiH@C_3N_4 anode, the polarization of the charge and discharge process for LiMg-LiH@C_3N_4||NCM811 full cell exhibits a superior stability with a much lower value that of bare Li||NCM811 full cell during the proceeding of cycling process (Figs. 5g and S23). To further investigate the potential application of LiMg-LiH@C_3N_4 under practical conditions, the N/P ratio of LiMg-LiH@g-C_3N_4||LFP and bare Li||LFP full cells is controlled to be 1.7 and 1.9, respectively, and the E/C ratio is reduced to about 5.7 μL (mA h)$^{-1}$. Upon cycling at 0.5 C (Fig. S24), bare Li||LFP full cells exhibited rapid capacity decay after only 58 cycles owing to the significant increase of loading ratio of LFP. In strong contrast, LiMg-LiH@C_3N_4||LFP full cells exhibited a stable cycling performance of over 150 cycles with a capacity retention of 93.6%. The excellent cycling stability of LiMg-LiH@C_3N_4||LFP indicates the potential practical application of LiMg-LiH@C_3N_4 anode. Moreover, Li||NCM811 pouch cells with a designed capacity of 780 mA h were assembled and investigated (Fig. S25). Upon charging at 0.5 C and discharging at 1 C, bare Li||NCM811 pouch cells exhibit rapid capacity decay after only 7 cycles toward battery failure, whereas LiMg-LiH@C_3N_4||NCM811 pouch cells exhibit a much better cycling stability with a capacity of 595.8 mA h after 14 cycles. The calculated overall energy density in weight and volume is approximately 291.9 W h kg^{-1} and 351.7 W h L^{-1}, respectively. This further confirms the potential application of LiMg-LiH@C_3N_4 anode under practical condition.

3. Conclusion

In conclusion, taking advantage of the favorable reaction between MgH_2@g-C_3N_4 and molten Li, a 3D structured LiMg-LiH@C_3N_4 anode

featured with uniform electron and Li ion conductive pathway is fabricated. The uniform formation of lithiophilic LiMg alloys under the structural support of lithiophilic g-C_3N_4 could synergistically lower the nucleation barrier of Li plating, which effectively promotes the uniform Li deposition process of LiMg-LiH@C_3N_4 anode. On the other hand, the high Li ion conductivity of LiH and Li_3N resulting from the reaction between molten Li and MgH_2 and g-C_3N_4, respectively, thermodynamically enhances the Li ion transportation kinetics along their surfaces towards favorable Li deposition on the surface of g-C_3N_4. In addition, the uniform distribution of g-C_3N_4 is able to act as stable structural support, which would mitigate the large volume change upon the repeated Li stripping and plating process and hence stabilize the formation of SEI layers. As a result, the thus-fabricated LiMg-LiH@C_3N_4 anode, which has a high specific capacity of 3511 mA h g^{-1}, delivers a long cycling life of over 500 h at 3 mA cm^{-2} with a fixed capacity of 3 mA h cm^{-2}. More importantly, when coupling LiMg-LiH@C_3N_4 anode with commercial LFP cathode, the thus-assembled full cell could deliver a specific capacity of 145 mA h g^{-1} after 450 cycles at 1 C, corresponding to a capacity retention of 94.2%. This proof-of-concept study in the design of electron and Li ion conductive pathway provides a fundamental and fresh insight into the development of stable Li metal anode, which could be further extended to the enhancement of Na or K metal anodes.

4. Experimental section/methods

4.1. Synthesis of g-C_3N_4

g-C_3N_4 was prepared *via* twice calcination assembly of lamella. Firstly, 5 g of urea was put into porcelain crucibles equally to be calcinated in a tube furnace at 550 °C under the atmosphere of nitrogen. The thus-obtained product was named as bulk g-C_3N_4. After cooling down to room temperature, bulk g-C_3N_4 was exfoliated into nanolamellar named g-C_3N_4 by calcination at 600 °C.

4.2. Preparation of MgH_2@g-C_3N_4, MgH_2 nanoparticles, and Mg@g-C_3N_4

MgH_2 nanoparticles supported on g-C_3N_4 were first synthesized via the hydrogenation-induced self-assembly method. In a typical fabrication process, 1.5 mL di-*n*-butylmagnesium (MgBu2) (1 M in heptane) and 28 mg C_3N_4 were added into a pressure reactor vessel, containing 40 mL cyclohexane. Subsequently, the self-assembly process was conducted at 200 °C under a hydrogen pressure of 40 atm for 24 h. After consecutive washing with anhydrous hexane and tetrahydrofuran followed by centrifugation, the thus-obtained products were vacuum-dried at 100 °C for 10 h on a Schlenk line to obtain MgH_2@g-C_3N_4. MgH_2 nanoparticles were synthesized by the same method without the addition of g-C_3N_4. The as-prepared MgH_2@g-C_3N_4 was dehydrogenated by thermal annealing to obtain Mg@ g-C_3N_4.

4.3. Preparation of LiMg-LiH@C_3N_4, LiMg-C_3N_4, LiMg-LiH, and Li@C_3N_4

A certain amount of MgH_2@g-C_3N_4 (2.5, 5, 7.5 and 10 wt.%) was dispersed uniformly on Li foil, followed by pressing and rolling for several times. Subsequently, these Li foils were heated at 280 °C to obtain LiMg-LiH@C_3N_4. Based on the cycling performance of the as-prepared anodes, the optimal adding content of MgH_2@g-C_3N_4 is 5 wt.% according to the symmetric cell test. The fabrication of LiMg-C_3N_4, LiMg-LiH, and Li@C_3N_4 was realized based on the same procedure using Mg@g-C_3N_4, MgH_2 nanoparticles, and g-C_3N_4, respectively, as the precursor. The as-prepared LiMg-LiH@C_3N_4, LiMg-C_3N_4, LiMg-LiH, or Li@C_3N_4 was pressed and cut into 12 mm-diameter electrodes for symmetric and full cell tests. In symmetric cell tests, the thickness of these 3D structured Li metal anode was controlled to be 150 μm. The areal capacity of LiMg-LiH@C_3N_4 and bare Li was approximately 27.3 and 30 mA h cm^{-2}, respectively. In Li||LFP (LFP: 10.5 mg cm^{-2}) and Li||NCM811 (10 mg cm^{-2}) full cells, the thickness of anode is controlled to be 150 μm. In Li||LFP (LFP: 31 mg cm^{-2}) full cells and pouch cells, the thickness of anode is controlled to be 50 μm.

4.4. Materials characterization

The phase composition of g-C_3N_4, MgH_2@g-C_3N_4, and LiMg-LiH@C_3N_4 was measured by X-ray diffraction (XRD, Bruker D8 Advance) with Cu Kα radiation ($\lambda = 1.5418$ Å). The morphology of as-prepared samples was determined with a scanning electron microscope (SEM, FEI Nova Nano 450) and a transmission electron microscope (TEM, JEOL 2011F). X-ray photoelectron spectroscopy (XPS, Thermo Scientific K-Alpha$^+$) experiments were performed with single X-ray source, using an Al Kα (1486 eV) anode. The pressure in analysis room during data acquisition was maintained at $\leq 2 \times 10^{-7}$ mbar. All binding energies were calibrated by using the contaminant carbon (C 1 *s* = 284.8 eV) as a reference.

4.5. Electrochemical measurement

The electrochemical performance was tested in CR2032 type coin cells with Celgard 2500 separator. 1 M lithium bis(trifluoromethane) sulfonimide (LiTFSI) in 1,3-dioxolane (DOL) and dimethoxyethane (DME) (1:1 in volume) with 0.2 M $LiNO_3$ was employed as the electrolyte of symmetric cells. 1 M lithium hexafluorophosphate ($LiPF_6$) in ethylene carbonate (EC) and diethyl carbonate (DEC) (1/1 in volume) with the addition of 10 wt.% fluoroethylene carbonate (FEC) and 1% vinylene carbonate (VC) was used as another electrolyte of full cells. The volume of electrolyte in each cell was controlled to be 40 μl. $LiNO_3$ and FEC were introduced in electrolyte to optimize SEI. In symmetric cells, Li metal electrodes (12 mm in diameter) were used as both working and counter electrodes. The LFP and NCM811 cathodes were purchased from Canrd (Guangdong Canrd New Energy Technology Co.,Ltd). In Li||LFP full cells, when the active mass loading of LFP cathode is 10.5 mg cm^{-2}, the E/C ratio in the full cell test of LFP is 22.4 μL (mA h)$^{-1}$ and the N/P ratio for LiMg-LiH@C_3N_4||LFP and bare Li||LFP is 15.3 and 16.8, respectively. When the active mass loading of LFP increases to 31 mg cm^{-2} and the electrolyte is controlled to be 30 μL, the E/C ratio is 5.7 μL (mA h)$^{-1}$ and the N/P ratio for LiMg-LiH@C_3N_4||LFP and bare Li||LFP is 1.7 and 1.9, respectively. In Li||NCM811 full cells, when the active mass loading of NCM811 cathode is 10 mg cm^{-2}, the E/C ratio in the full cell test of NCM811 is 23.5 μL (mA h)$^{-1}$ and the N/P ratio for LiMg-LiH@C_3N_4||NCM811 and bare Li||NCM811 is 16.1 and 17.6, respectively. The pouch cells were assembled by pairing double-sided NCM811 cathodes (2.72 mA h cm^{-2} on each side; size: 5.4 cm × 5.2 cm) with Li metal anodes (thickness: 50 μm; size: 5.6 cm × 5.4 cm). The E/C ratio in the pouch test is 1.6 μL (mA h)$^{-1}$ and the N/P ratio for LiMg-LiH@C_3N_4||NCM811 and bare Li||NCM811 is 1.7 and 1.8, respectively.

The galvanostatic charge/discharge measurements of symmetric cells and full cells were carried out on a LAND battery testing system at room temperature. The voltage window for Li//LFP and Li//NCM811 full cells was set to be 2.5 - 4 V and 3 - 4.3 V, respectively. The electrochemical impedance spectroscopy (EIS) measurements were performed in the frequency range of 100 kHz to 0.1 Hz. Linear sweep voltammetry (LSV) was conducted at a fixed sweep rate of 1 mV s^{-1} with the voltage range from −200 mV to 200 mV. The corresponding exchange current density was calculated by linear fitting (from −150 mV to −100 mV). Both EIS and LSV measurements were conducted on a SP-300 electrochemical workstation (Bio-Logic).

4.6. Theoretical calculation

Density functional theory (DFT) calculations were carried out using projector-augmented wave (PAW) method as implemented in Vienna ab initio simulation package (VASP) [42–44]. A generalized gradient

approximation (GGA) of Perdew-Burke-Ernzerhof (PBE) functional was utilized to describe the exchange-correlation interaction [45]. The van der Waals (vdW) correction DFT-D3 proposed by Grimme was employed to describe the dispersion interaction [46]. The energy cutoff was set to 500 eV. Spin polarization and Gamma centered $3 \times 3 \times 1$ k-points mesh were applied to all calculations. Li_3N (100), Li_7Mg (001), and LiH (001) were selected to simulate the interfaces in the electrode. The vacuum layer of 20 Å was adopted in all calculations. The structures were relaxed until the forces and total energy on all atoms were converged to less than 0.05 eV $Å^{-1}$ and 1×10^{-5} eV. To evaluate the interaction between Li and the electrode, the binding energy (E_b) was calculated as follows,

$$E_b = E_{Total} - E_{Li} - E_{sub}$$

where E_{sub} and E_{Total} are the total energy of compound before and after Li deposition, respectively. E_{Li} is the energy of a single Li atom. A lower the binding energy suggest that the interaction between Li and electrode is stronger. Activation barriers for deposited Li hopping between adjacent interstitial sites in the interfaces were calculated using the climbing-image nudged elastic band (CI-NEB) method [47].

CRediT authorship contribution statement

Hongyu Zhang: Investigation, Formal analysis, Writing – original draft. **Yanran Wang:** Investigation, Methodology, Writing – original draft. **Shunlong Ju:** Investigation, Formal analysis. **Panyu Gao:** Investigation. **Tongxin Zou:** Investigation. **Tianren Zhang:** Investigation. **Juan Wang:** Investigation. **Guanglin Xia:** Supervision, Conceptualization, Methodology, Writing – review & editing. **Xuebin Yu:** Supervision, Conceptualization, Methodology, Writing – review & editing.

Declaration of Competing Interest

The authors declare that they have no known competing financial interests or personal relationships that could have appeared to influence the work reported in this paper.

Acknowledgements

This work was partially supported by the National Key R&D Program of China (No. 2020YFA0406204), National Science Fund for Distinguished Young Scholars (51625102), the National Natural Science Foundation of China (51971065, 51901045, U2130208), the Science and Technology Commission of Shanghai Municipality (No. 21ZR1407500), and the Innovation Program of Shanghai Municipal Education Commission (2019–01–07–00–07-E00028), and the Programs for Professor of Special Appointment (Eastern Scholar) at Shanghai Institutions of Higher Learning.

Supplementary materials

Supplementary material associated with this article can be found, in the online version, at doi:10.1016/j.ensm.2022.08.001.

Reference

[1] J.W. Choi, D. Aurbach, Promise and reality of post-lithium-ion batteries with high energy densities, Nat. Rev. Mater. 1 (2016) 16013.
[2] J.B. Goodenough, Y. Kim, Challenges for rechargeable Li batteries, Chem. Mater. 22 (2010) 587–603.
[3] M.M. Thackeray, C. Wolverton, E.D. Isaacs, Electrical energy storage for transportation—approaching the limits of, and going beyond, lithium-ion batteries, Energy Environ. Sci. 5 (2012) 7854–7863.
[4] P.-.Y. Zhai, H.-.J. Peng, X.-.B. Cheng, L. Zhu, J.-.Q. Huang, W. Zhu, Q. Zhang, Scaled-up fabrication of porous-graphene-modified separators for high-capacity lithium–sulfur batteries, Energy Storage Mater 7 (2017) 56–63.
[5] X.-.B. Cheng, R. Zhang, C.-.Z. Zhao, Q. Zhang, Toward safe lithium metal anode in rechargeable batteries: a review, Chem. Rev. 117 (2017) 10403–10473.
[6] L. Suo, Y.-.S. Hu, H. Li, M. Armand, L. Chen, A new class of solvent-in-salt electrolyte for high-energy rechargeable metallic lithium batteries, Nat. Commun. 4 (2013) 1481.
[7] M.S. Kim, J.-.H. Ryu, Deepika, Y.R. Lim, I.W. Nah, K.-.R. Lee, L.A. Archer, W. Il Cho, Langmuir–blodgett artificial solid-electrolyte interphases for practical lithium metal batteries, Nat. Energy 3 (2018) 889–898.
[8] J. Liu, Z. Bao, Y. Cui, E.J. Dufek, J.B. Goodenough, P. Khalifah, Q. Li, B.Y. Liaw, P. Liu, A. Manthiram, Y.S. Meng, V.R. Subramanian, M.F. Toney, V. V. Viswanathan, M.S. Whittingham, J. Xiao, W. Xu, J. Yang, X.-.Q. Yang, J.-. G. Zhang, Pathways for practical high-energy long-cycling lithium metal batteries, Nat. Energy 4 (2019) 180–186.
[9] H. Zhang, G.G. Eshetu, X. Judez, C. Li, L.M. Rodriguez-Martínez, M. Armand, Electrolyte additives for lithium metal anodes and rechargeable lithium metal batteries: progress and perspectives, Angew. Chem. Int. Ed. 57 (2018) 15002–15027.
[10] P. Zhai, L. Liu, X. Gu, T. Wang, Y. Gong, Interface engineering for lithium metal anodes in liquid electrolyte, Adv. Energy. Mater. 10 (2020), 2001257.
[11] C. Yang, K. Fu, Y. Zhang, E. Hitz, L. Hu, Protected lithium-metal anodes in batteries: from liquid to solid, Adv. Mater. 29 (2017), 1701169.
[12] B. Liu, J.-.G. Zhang, W. Xu, Advancing lithium metal batteries, Joule 2 (2018) 833–845.
[13] Y. Zhao, Y. Ye, F. Wu, Y. Li, L. Li, R. Chen, Anode interface engineering and architecture design for high-performance lithium–sulfur batteries, Adv. Mater. 31 (2019), 1806532.
[14] X.-.B. Cheng, R. Zhang, C.-.Z. Zhao, F. Wei, J.-.G. Zhang, Q. Zhang, A review of solid electrolyte interphases on lithium metal anode, Adv. Sci. 3 (2016), 1500213.
[15] D.-.H. Liu, Z. Bai, M. Li, A. Yu, D. Luo, W. Liu, L. Yang, J. Lu, K. Amine, Z. Chen, Developing high safety Li-metal anodes for future high-energy li-metal batteries: strategies and perspectives, Chem. Soc. Rev. 49 (2020) 5407–5445.
[16] S. Ye, L. Wang, F. Liu, P. Shi, H. Wang, X. Wu, Y. Yu, g-C_3N_4 derivative artificial organic/inorganic composite solid electrolyte interphase layer for stable lithium metal anode, Adv. Energy. Mater 10 (2020), 2002647.
[17] N.-.W. Li, Y. Shi, Y.-.X. Yin, X.-.X. Zeng, J.-.Y. Li, C.-.J. Li, L.-.J. Wan, R. Wen, Y.-. G. Guo, A flexible solid electrolyte interphase layer for long-life lithium metal anodes, Angew. Chem. Int. Ed. 57 (2018) 1505–1509.
[18] Y. Guo, P. Niu, Y. Liu, Y. Ouyang, D. Li, T. Zhai, H. Li, Y. Cui, An autotransferable g-C_3N_4 Li^+-modulating layer toward stable lithium anodes, Adv. Mater. 31 (2019), 1900342.
[19] J. Xie, L. Liao, Y. Gong, Y. Li, F. Shi, A. Pei, J. Sun, R. Zhang, B. Kong, R. Subbaraman, J. Christensen, Y. Cui, Stitching h-BN by atomic layer deposition of LiF as a stable interface for lithium metal anode, Sci. Adv. 3 (2017) eaao3170.
[20] S.T. Oyakhire, W. Huang, H. Wang, D.T. Boyle, J.R. Schneider, C. de Paula, Y. Wu, Y. Cui, S.F. Bent, Revealing and elucidating ALD-derived control of lithium plating microstructure, Adv. Energy. Mater. 10 (2020), 2002736.
[21] M. Wan, S. Kang, L. Wang, H.-.W. Lee, G.W. Zheng, Y. Cui, Y. Sun, Mechanical rolling formation of interpenetrated lithium metal/lithium tin alloy foil for ultrahigh-rate battery anode, Nat. Commun. 11 (2020) 829.
[22] D. Lin, J. Zhao, J. Sun, H. Yao, Y. Liu, K. Yan, Y. Cui, Three-dimensional stable lithium metal anode with nanoscale lithium islands embedded in ionically conductive solid matrix, Proc. Natl. Acad. Sci. 114 (2017) 4613.
[23] H. Wang, D. Lin, Y. Liu, Y. Li, Y. Cui, Ultrahigh current density anodes with interconnected Li metal reservoir through overlithiation of mesoporous AlF_3 framework, Sci. Adv 3 (2017), e1701301.
[24] P. Shi, T. Li, R. Zhang, X. Shen, X.-.B. Cheng, R. Xu, J.-.Q. Huang, X.-.R. Chen, H. Liu, Q. Zhang, Lithiophilic LiC_6 layers on carbon hosts enabling stable Li metal anode in working batteries, Adv. Mater. 31 (2019), 1807131.
[25] S.-.S. Chi, Q. Wang, B. Han, C. Luo, Y. Jiang, J. Wang, C. Wang, Y. Yu, Y. Deng, Lithiophilic Zn sites in porous CuZn alloy induced uniform Li nucleation and dendrite-free Li metal deposition, Nano Lett 20 (2020) 2724–2732.
[26] W. Zhu, W. Deng, F. Zhao, S. Liang, X. Zhou, Z. Liu, Graphene network nested Cu foam for reducing size of lithium metal towards stable metallic lithium anode, Energy Storage Mater 21 (2019) 107–114.
[27] X.-.Y. Yue, Q.-.Y. Zhou, J. Bao, C. Ma, S.-.Y. Yang, X.-.L. Li, D. Sun, F. Fang, X.-. J. Wu, Y.-.N. Zhou, In situ construction of lithium silicide host with unhindered lithium spread for dendrite-free lithium metal anode, Adv. Funct. Mater. 31 (2021), 2008786.
[28] W. Guo, S. Liu, X. Guan, X. Zhang, X. Liu, J. Luo, Mixed ion and electron-conducting scaffolds for high-rate lithium metal anodes, Adv. Energy. Mater. 9 (2019), 1900193.
[29] S. Gao, X. Wang, C. Song, S. Zhou, F. Yang, Y. Kong, Engineering carbon-defects on ultrathin g-C_3N_4 allows one-pot output and dramatically boosts photoredox catalytic activity, Appl. Catal., B 295 (2021), 120272.
[30] G. Xia, Y. Tan, X. Chen, D. Sun, Z. Guo, H. Liu, L. Ouyang, M. Zhu, X. Yu, Monodisperse magnesium hydride nanoparticles uniformly self-assembled on graphene, Adv. Mater. 27 (2015) 5981–5988.
[31] Z. Peng, J. Song, L. Huai, H. Jia, B. Xiao, L. Zou, G. Zhu, A. Martinez, S. Roy, V. Murugesan, H. Lee, X. Ren, Q. Li, B. Liu, X. Li, D. Wang, W. Xu, J.-.G. Zhang, Enhanced stability of Li metal anodes by synergetic control of nucleation and the solid electrolyte interphase, Adv. Energy. Mater. 9 (2019), 1901764.
[32] H. Zhang, S. Ju, G. Xia, D. Sun, X. Yu, Dendrite-free Li-metal anode enabled by dendritic structure, Adv. Funct. Mater. 31 (2021), 2009712.
[33] T. Zhang, H. Lu, J. Yang, Z. Xu, J. Wang, S.-i. Hirano, Y. Guo, C. Liang, Stable lithium metal anode enabled by a lithiophilic and electron/ion conductive framework, ACS Nano 14 (2020) 5618–5627.

[34] L. Fu, X. Wang, L. Wang, M. Wan, Y. Li, Z. Cai, Y. Tan, G. Li, R. Zhan, Z.W. Seh, Y. Sun, A salt-in-metal anode: stabilizing the solid electrolyte interphase to enable prolonged battery cycling, Adv. Funct. Mater. 31 (2021), 2010602.
[35] Z. Peng, F. Ren, S. Yang, M. Wang, J. Sun, D. Wang, W. Xu, J.-.G. Zhang, A highly stable host for lithium metal anode enabled by Li_9Al_4-Li_3N-AlN structure, Nano Energy 59 (2019) 110–119.
[36] H. Qiu, T. Tang, M. Asif, W. Li, T. Zhang, Y. Hou, Stable lithium metal anode enabled by lithium metal partial alloying, Nano Energy 65 (2019), 103989.
[37] D. Lu, Y. Shao, T. Lozano, W.D. Bennett, G.L. Graff, B. Polzin, J. Zhang, M. H. Engelhard, N.T. Saenz, W.A. Henderson, P. Bhattacharya, J. Liu, J. Xiao, Failure mechanism for fast-charged lithium metal batteries with liquid electrolytes, Adv. Energy. Mater. 5 (2015), 1400993.
[38] Y.-.X. Zhan, P. Shi, X.-.X. Ma, C.-.B. Jin, Q.-.K. Zhang, S.-.J. Yang, B.-.Q. Li, X.-. Q. Zhang, J.-.Q. Huang, Failure mechanism of lithiophilic sites in composite lithium metal anode under practical conditions, Adv. Energy. Mater. 12 (2022), 2103291.
[39] C.-.B. Jin, X.-.Q. Zhang, O.-.W. Sheng, S.-.Y. Sun, L.-.P. Hou, P. Shi, B.-.Q. Li, J.-. Q. Huang, X.-.Y. Tao, Q. Zhang, Reclaiming inactive lithium with a triiodide/iodide redox couple for practical lithium metal batteries, Angew. Chem. Int. Ed. 60 (2021) 22990–22995.
[40] M. Chen, J. Zheng, Y. Liu, O. Sheng, Z. Ju, G. Lu, T. Liu, Y. Wang, J. Nai, Q. Wang, X. Tao, Marrying ester group with lithium salt: cellulose-acetate-enabled LiF-enriched interface for stable lithium metal anodes, Adv. Funct. Mater. 31 (2021), 2102228.
[41] E. Nasybulin, W. Xu, M.H. Engelhard, Z. Nie, S.D. Burton, L. Cosimbescu, M. E. Gross, J.-.G. Zhang, Effects of electrolyte salts on the performance of Li–O_2 batteries, J. Phys. Chem. C 117 (2013) 2635–2645.
[42] G. Kresse, J. Furthmüller, Efficient iterative schemes for ab initio total-energy calculations using a plane-wave basis set, Phys. Rev. B 54 (1996) 11169.
[43] G. Kresse, Ab initio molecular dynamics for liquid metals, J. Non. Cryst. Solids 192-193 (1995) 222–229.
[44] P.E. Blöchl, Projector augmented-wave method, Phys. Rev. B 50 (1994) 17953–17979.
[45] J.P. Perdew, K. Burke, M. Ernzerhof, Generalized gradient approximation made simple, Phys. Rev. Lett. 77 (1996) 3865–3868.
[46] S. Grimme, J. Antony, S. Ehrlich, H. Krieg, A consistent and accurate ab initio parametrization of density functional dispersion correction (DFT-D) for the 94 elements H-Pu, J. Chem. Phys. 132 (2010), 154104.
[47] G. Henkelman, H. Jónsson, Improved tangent estimate in the nudged elastic band method for finding minimum energy paths and saddle points, J. Chem. Phys. 113 (2000) 9978–9985.